IEEE Access
Multidisciplinary : Rapid Review : Open Access Journal

Received November 1, 2021, accepted November 18, 2021, date of publication November 23, 2021, date of current version December 6, 2021.

Digital Object Identifier 10.1109/ACCESS.2021.3130371

Detection of Refractive Index With a Temperature-Compensated MZI-Based Optical Sensor Using Few-Mode Fiber

BIN-ZHOU ZUO[1], XIAO LIANG[1], XU-RAN ZHANG[1], AND TIAN-HE YIN[2]

[1]School of Information Engineering, Minzu University of China, Beijing 100081, China
[2]School of Foreign Studies, Minzu University of China, Beijing 100081, China

Corresponding author: Xiao Liang (bjtulxlx@sina.com)

This work was supported in part by the National Natural Science Foundation of China under Grant 61905293, and in part by the Young Teachers Research Ability Enhancement Project at the Minzu University of China under Grant 2021QNPY114.

ABSTRACT A temperature-compensated MZI-based optical sensor using few-mode concentric multilayer-core fiber (CMCF) was designed, and surrounding refractive index (SRI) sensing via interference spectra was successfully proposed and experimentally demonstrated. This sensor with sandwich structure generated lots of resonance dips in the interference spectra, which had differentiated sensitivities to SRI and temperature. The homemade CMCF only supported few mode groups, and variability of the resonance drift could be influenced by different mode excitation and sensitivity. For the two selected dips of this proposed sensor, the SRI sensitivities experimentally achieved were −76.88 and −50.51 nm per refractive index unit (RIU), and the temperature ones were 80.2 and 50.1 pm/°C, respectively. The experimental mechanism and results have been analyzed in brief. The standard matrix inversion method could be used for simultaneous two parameter determination. Therefore, the SRI detection could show good accuracy and sensitivity by temperature compensation.

INDEX TERMS Dual-mode fiber, fiber sensor, MZI, temperature-compensated, cross sensitivity.

I. INTRODUCTION

Over the years, measurement of surround refractive index (SRI) is increasingly essential in many fields, such as medical biology, environmental monitoring, aerospace, construction industry and meteorological services [1]–[4]. Fiber-optic sensors possess good application prospects in SRI measuring, and have drawn a great deal of attention due to several inherently distinctive features, such as low weight, compact size, anti-erosion, chemical and biological inert, immunity to electromagnetic interference and remote operation [5]–[7]. However, due to the thermal-optical effect, the fiber-optic sensor is also sensitive to temperature, and it is difficult to make very precise measurements of SRI. The general effect on the temperature in fiber sensors has been widely perceived as an engineering problem that limits the sensing applications. To solve the cross-sensitivity problem, temperature-compensated optical fiber sensors have attained increasing attention in monitoring SRI, which can provide a very precise measurement [5], [8].

The associate editor coordinating the review of this manuscript and approving it for publication was Muguang Wang.

Several SRI fiber sensors without temperature interference have been proposed, which can be approximately classified into two categories: temperature-insensitive ones and temperature-compensated ones. In the former case, the sensor is only interested in SRI, and is indifferent to temperature. Weng *et al.* proposed a double-side polished fiber sensor based on surface plasmon resonance (SPR) which could measure the temperature and SRI simultaneously by monitoring the resonant wavelength shifts of x- and y-polarized loss spectrums. But the temperature sensitivity of y-polarized loss spectrum is very low, which could probably be negligible. As a result of being almost insensitive to temperature, this sensor could measure SRI effectively [9]. Zhou *et al.* reported a micro-structural SRI probe with negligible temperature crosstalk, which could transform the measured wavelength shift into SRI using the calibrated data without any modification [10]. As noted above, both of them are slightly sensitive to temperature and then bring negligible cross-talk

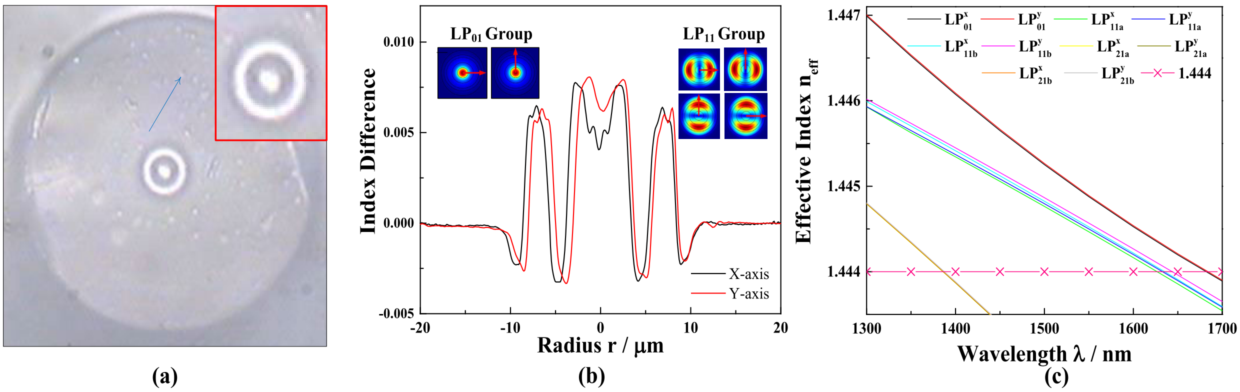

FIGURE 1. Schematic diagrams of (a) the cross-section micrograph of the CMCF; (b) index profile of the CMCF, the insets show the supported mode groups; and (c) the dispersion curves of the supported modes.

between RI and temperature, as well as involving relatively complex fabrication process. Apparently, these sensors are not so absolutely insensitive to temperature, which could bring the interference to SRI survey, as to make unnecessary troubles in implementing effective precise measurement to SRI. In the second case, the sensor could acquire both the changes of the SIR and temperature along fibers, and has different sensing behaviors to them. Hence, such dual-parameter sensors have different sensitivities for SRI and temperature, and could show good accuracy and sensitivity to SRI by temperature compensation. Kinds of the temperature-compensated SRI-sensor configurations have been proposed, such as hybrid single-mode fiber (SMF) structure [11], SPR [12], [13], a fiber Bragg grating (FBG) [14], [15], a long-period grating, photonic crystal fiber (PCF) [16], Fabry-Perot (FP) interferometer [17], [18], Sagnac interferometer [19], tapers [20], [21], dual-microspheric structure [22] and Mach-Zehnder (MZ) interferometer [23], [24].

In this research, a method to probe the SRI on the basis of a temperature-compensated MZI-based optical sensor using few-mode concentric multilayer-core fiber (CMCF) is proposed and experimentally characterized. The temperature disturbance is vital factors affecting the performance of fiber sensors. According to the results of sensing experiments, the sensing property of transmission dips in the MZI-based sensor will perform varying degrees of deviation with SRI and temperature. The two transmission dips could have different sensing behaviors. Therefore, the proposed MZI-based optical sensor can measure the SRI without temperature cross-sensitivity. To the best of my knowledge, the detailed characteristic of the interference waveforms under different mode intensity is firstly analyzed. The propagation characteristic and operation mechanism of this advanced sensor is introduced meticulously.

II. DESIGN AND PRINCIPLES OF OPERATION

A. STRUCTURE OF THE CMCF

In order to make sure the sensor is able to get a clear interference spectrum, our research team took advantage of conventional modified chemical vapor deposition (MCVD) and solution-doping techniques to produce a special structure fiber, CMCF, which can ensure the targeted wavelength only inspires two modes with similar amount of energy. Fig. 1 (a) describes the micro-cross-section of CMCF, which consists of a circular core area on the inside and a cladding on the outside. The white part of the fiber core consists the high refractive index layer, which is made by doping germanium. The gray part represents the low refractive index layer, which is synthesized by doping fluoride. The out layer of the fiber core is a cladding consisting of pure silica with a refractive index of 1.444. Fig.1 (b) is the refractive index profile obtained by the fiber refractive index analyzer (EXFO's NR9200). The positive refractive index difference in the core region can reach nearly 8×10^{-3}, while the negative refractive index difference can reach nearly -3.4×10^{-3}. Furthermore, the refractive indexes along the x-axis and the y-axis do not completely correspond with each other, which is the key to CMCF's ability to produce both modes. Asymmetry of the index profiles has been introduced in the MCVD process, which would cause the offset coupling of the incident beam naturally [25], [26]. And the excitation of higher-order modes would be easy to implement. Fig.1 (c) shows the relationship between the wavelength and the effective refractive indexes of some mode groups. Our research team found that only two modes, LP_{01} and LP_{11}, can propagate in 1390 and 1630 nm regions. The refractive indexes measured along the x-axis and y-axis are not exactly symmetrical in geometry morphology, resulting in the four dispersion curves of LP_{11} and the two dispersion curves of LP_{01} not fully coincide.

B. CONFIGURATION OF THE SENSOR AND TRANSMISSION PRINCIPLE

Fig. 2 shows a structure diagram of the sensor head, which is made of CMCF-based fibers, playing the role of the MZI. It constructs the CSC structure by stitching a segment of the SMF (corning SMF-28) between two CMCF fragments of the same size using the fiber fusion splicer (Fujikura, FSM-100M/P). The CMCF fragment, shown in Fig.2, plays the role of a pattern generator and coupler; the middle SMF acts as the arm of the MZI, and the SMFs on both sides work as the signal

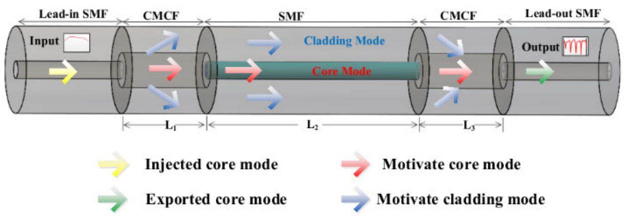

FIGURE 2. **Schematic representation and operation of the sensor head.**

input and output. Because of difference between the SMF and CMCF in the mode field distribution, mode mismatch occurs at the fusion points. This specially designed practice can excite a couple of higher-order modes. The coatings are obtained on the SMF, whose refractive index is higher than fiber cladding, and it can absorb the radiation modes in fibers, which means only fundamental mode could propagate in it. By removing the coating of the CSC structure completely, when the Gaussian beam passes through the first CMCF from the lead-in SMF, it excites the higher-order mode which propagates in the cladding of SMF, and meets the fundamental mode which is coupled in the core area at the second CMCF. Due to the optical path difference between the fundamental mode and LP_{11}, a clean interference spectrum could be obtained. The loss caused by splicing between CMCF and SMF are between 0.7dB and 1.03dB, which has little effect on actual measurements. Both CMCFs are 4.5 mm; the center SMF is 50 mm, and the overall length is only 59 mm. The half beat length L_π is determined by the propagation coefficient β, according to basic geometrical optics equation

$$L_\pi = \frac{\pi}{\Delta\beta} \tag{1}$$

$\Delta\beta$ is the difference of the propagation constants of LP_{11} and LP_{01}. Half of the L_π is approximately 0.895mm, which is about one fifth of that of CMCF, and the two guided modes would be excited uniformly. As a consequence, the output spectrum could achieve a clear and clean spectrum. Meanwhile, due to the terse structure, there is a great potential for development and application in the multipoint sensing system.

When the excitation coefficients of the fundamental mode and LP_{11} are dominant and close to each other, the output pattern is usually clean and stabilized. According to the weakly-guiding approximation, and ignoring the loss of the radiation modes, the normalized distribution of the incident light, $\psi(x, y, z)$, can be expressed as

$$\psi(x, y, z) = \sum_{1}^{N} \eta_n \psi_n^{CMCF}(x, y) e^{-i\beta z} \tag{2}$$

N is the number of the excited modes. η_{n} is the excitation coefficient of the nth order mode in the CMCF, and ψ_n^{CMCF} is the guided mode distribution. When there are mainly two modes, the fundamental mode and the LP_{11}, N can be equaled to 1. β is the propagation coefficient. η_n is determined by the guided mode and injected field distribution. The excitation coefficient governed by the incident filed and the dominant mode distribution, can be calculated by two-dimension overlap integral as follows

$$\eta_{\mathrm{n}} = \frac{\iint \psi_{in}^{SMF}(x, y)\psi_n^{CMCF}(x, y)dxdy}{\iint \psi_n^{CMCF}(x, y)\psi_n^{CMCF}(x, y)dxdy} \tag{3}$$

ψ_{in}^{SMF} is the incident filed distribution.

Fig. 3(a) describes the excitation coefficients of the LP_{01} mode group and LP_{11} mode group respectively, which are determined by (3). The sum of the excitation coefficients is approximately equal to 1, indicating that there are almost only two guided modes supported by the CMCF. And the excitation coefficients of LP_{01} and LP_{11} are close to each other, which is essential for high output spectral extinction ratio. That is to say, this CSC structure is conducive to producing a clear output pattern. There are, of course, some other high-order modes whose power in the sensor would be very low, and they have minimal effect on the interference and sensing. Hence, the interference in this sensor would be approximately dual-mode operation. Fig.3 (b) and (c) show the field evolution and the normalized power along the z axis in liquid and air, respectively. As shown in Fig.3 (b), the energy is concentrated around the core and the evanescent wave caused by a small number of high-order modes is so weak that can be neglected in experiments. Fig.3 (c) shows that the sensor has a higher profile value in the air than in liquids due to a larger refractive index difference.

Because there are only two dominated interference modes coupled in the CSC based MZI, the output result can be seen as a simple dual-mode interference process. The distance between the two resonance dips, as the free spectral range (FSR) can be described as

$$FSR = \frac{\lambda^2}{\Delta n_{LP}^{SMF} L_{SMF} + 2\Delta n_{LP}^{CMCF} L_{CMCF}} \tag{4}$$

In SMF, n_{LP01}^{SMF} and n_{LP11}^{SMF} are the effective index of the two modes respectively, while n_{LP01}^{CMCF} and n_{LP11}^{CMCF} are the effective index of the two modes respectively. Δn_{LP}^{SMF} represents the difference between n_{LP01}^{SMF} and n_{LP11}^{SMF}, while Δn_{LP}^{CMCF} is the difference between n_{LP01}^{CMCF} and n_{LP11}^{CMCF}. L_{SMF}/L_{CMCF} is the effective length of SMF / CMCF.

By (4) our research team could know the value of FSR in air and water are 7.5 nm and 6.7 nm respectively. The measured transmission spectrums of the CMCF-based modal interferometer are depicted in Fig. 4(a), which are stable and clean due to the few-mode property. To investigate the stability of the interferometer, the spectrums have barely budged with repeated spectrometer scans for an hour, and the difference is difficult to find. The experiment result is quite close to the calculation of (4), indicating that a small number of higher order modules has no obvious effect on the output pattern. The output data is processed by Fourier transform (FFT) and the results are shown in Fig. 4(b). As seen, the spatial frequency spectrum of the MZI mainly has two peaks, which represents the fundamental mode and the LP_{11} respectively.

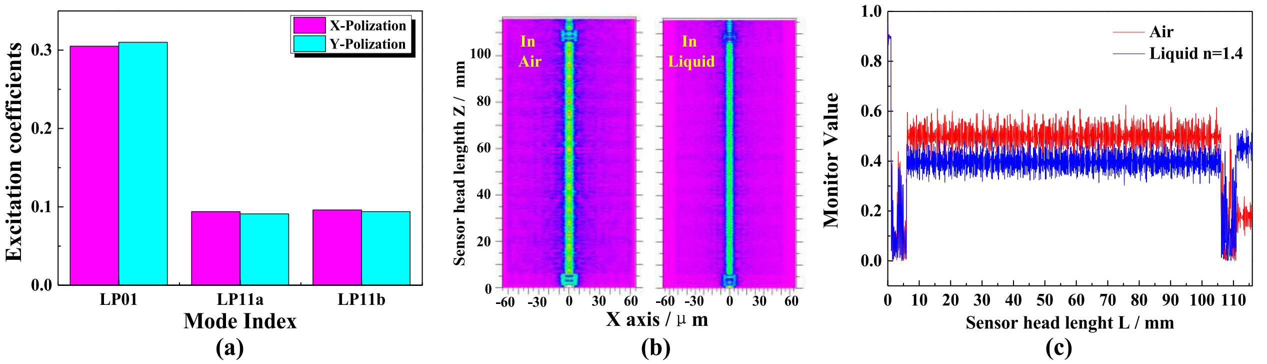

FIGURE 3. (a) Excitation coefficients for different modes; (b) Contour map of the beam propagation along the sensor head in air and liquid; (c) normalized power along the sensor head.

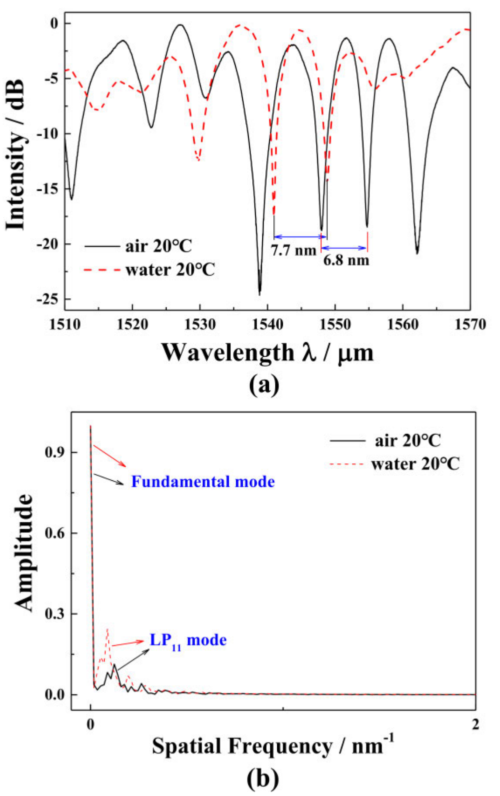

FIGURE 4. Interference-pattern analysis: (a) measured transmission spectrum of the CMCF-based modal interferometer, and (b) spatial frequency of these spectra.

The other peaks corresponding to higher-order modes are so weak that they would be neglected. The principal reason is that the coating of the CSC structure is removed completely, and the higher-order modes would be excited, which propagates in the cladding of SMF. However most of them would be evanescent waves and disappeared after propagating a distance. That is to say, there are only two major mode groups interfered in this MZI-based fiber sensor. The guided modes in the fiber sensor would be sensitivity to the surroundings influence. Obviously, the more modes the sensor has, the harder to control the interference spectrum would be. This is a requisite for a clean and stable output pattern. And the FSR is wider than that of multiple-mode interference, which would provide a large sensing range. The resonance dips for sensing would be conducive to facile distinction because of the clean interference spectrum, and the demodulation method would be simple, accurate and easy to operate. Finally, big range and high accuracy would be obtained.

C. SENSING PRINGCIPLE

This MZI-based fiber sensor could be susceptible to the surrounding temperature and RI, which is hinged on the dips of the interference spectrum. After removing the coating, the cladding effective refractive index n_{eff}^{cl} of this MZI-based senor could be affected by SRI, while the core effective refractive index n_{eff}^{co} would be hardly changed for the deep location. When the disturbance only caused by the RI changes of liquid samples, it is easy to have the functional relationship between the Nth resonant wavelength of mode m, λ_N^m, and SRI as follows

$$\Delta\lambda_N^m = \frac{2(\Delta n_{eff}^{co} - \Delta n_{eff}^{cl})L_{SMF}}{2N+1} \approx \frac{-2\Delta n_{eff}^{cl} L_{SMF}}{2N+1} = \frac{-2KL_{SMF}}{2N+1}\Delta n = Q_N^m \Delta n \tag{5}$$

$\Delta\lambda_N^m$ is the wavelength shifts of λ_N^m. N is the number of the resonant wavelengths. $\Delta n_{eff}^{cl}/\Delta n_{eff}^{co}$ is the refractive index change of the cladding / core in the middle SMF. Q_N^{m} is a constant. Δn is the refractive index change of the SRI. Therefore, the shift wavelength could be expressed as follows

$$\lambda_N = \lambda_{N,0} + \Delta\lambda_N^m \tag{6}$$

λ_N and $\lambda_{N,0}$ are the resonance dips before and after the SRI changes respectively. Our research team could find out that there is a linear relationship between wavelength drifts of mode m and SRI. In the following part, the SRI sensing characteristics of the MZI-based sensor made of a certain fiber parameter are simulated by Finite difference time domain (FDTD) method. Parts of the simulation result are given in the Fig. 5(a) and (c). Fig. 5(a) describes the blueshift of the interference spectrum as the SRI increasing (1.333, 1.343, 1.353, 1.363, 1.373). Fig. 5(c) shows the

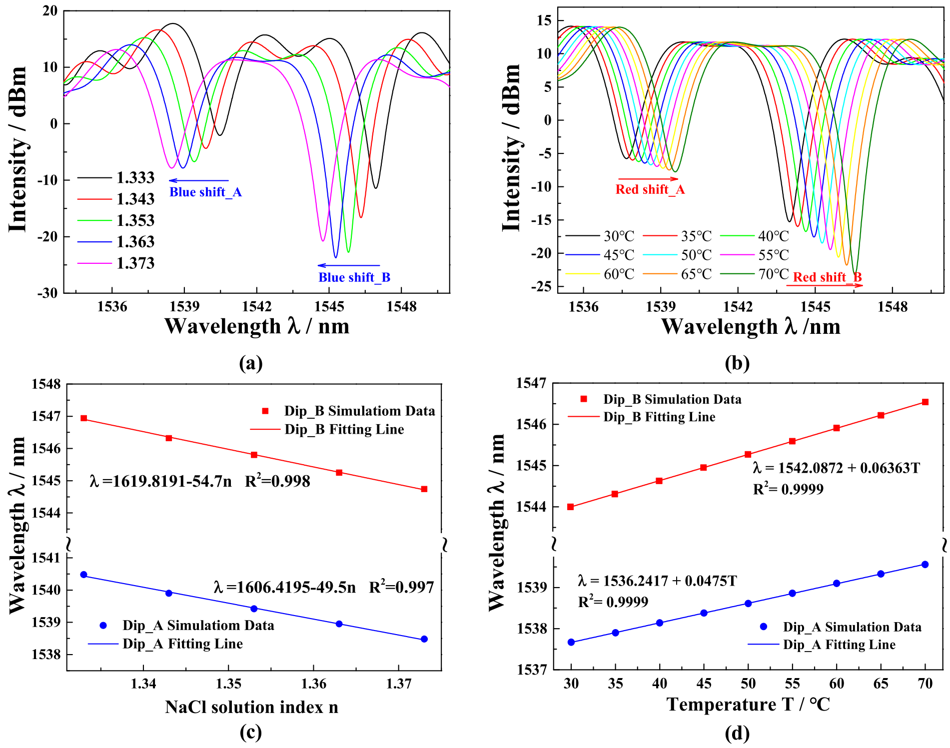

FIGURE 5. The simulation spectra of this senor under (a) different refractive index and (b) different surrounding temperature; the fitted result of dips wavelength shifts in response to (c) the refractive index change and (d)the temperature change.

SRI sensitivity for each dip, −54.7nm/RIU and −49.5nm/RIU, respectively. The correlation coefficients R^2 for linear fitting are 0.998 and 0.997 respectively, demonstrating the SRI is linearly related to the wavelength drifts. Analysis of this data shows that the experimental results are with high sensitivity and linearity.

When the disturbance only caused by the changing of the temperature, the influence caused by surrounding temperature can be mainly divided into thermo-optic effect and thermal expansion, minimally affected by other factors. Thermo-optic effect means that the RI of materials could be influenced by the surrounding temperature changes, while thermal expansion means that the general increase in the volume of a material as its temperature is increased. The exact relationships are given as follows

$$\zeta = \frac{1}{n}\frac{dn}{dT} \tag{7}$$

$$\sigma = \frac{1}{L}\frac{dL}{dT} \tag{8}$$

ζ is thermal optical coefficient, which represents the sensitivity of thermal-optical effect; σ is the dilatation coefficient, which indicates the sensitivity of thermal expansion. n is the RI of the fiber; T is the surrounding temperature. L is the effective length of the MZI-based interferometer. ζ and σ can be regarded two constants. L_{SMF}, n_{eff}^{co} and n_{eff}^{cl} are related with T, which could be expressed as $dL_{SMF}(T) = L_{SMF}dT$, $dn_{eff}^{co} = n_{eff}^{co}dT$, $dn_{eff}^{cl} = n_{eff}^{cl}dT$ respectively. (9) can be derived from (6) by simple algebraic transformations as follows [3], [27]

$$\lambda_N^m = \frac{2(n_{eff}^{co} - n_{eff}^{cl})L_{SMF}}{2N+1} \tag{9}$$

Taking the derivative of this expression, we can get

$$d\lambda_N^m = \frac{2}{2N+1} * [(n_{eff}^{co} - n_{eff}^{cl})dL_{SMF} + (dn_{eff}^{co} - dn_{eff}^{cl})L_{SMF}] \tag{10}$$

when the surrounding temperature is uniform for the whole the MZI-based sensor, combining (7), (8) and (10), we could evaluate the temperature susceptibility of wavelength dips.

$$G_T^m = \frac{d\lambda_N^m}{dT} = \frac{2(n_{eff}^{co} - n_{eff}^{cl})L_{SMF}}{2N+1}(\sigma + \zeta) \tag{11}$$

G_T^m is the temperature coefficient of this fiber sensor. It is easy to find out that G_T^m is a constant, indicating that the Nth dips of mode m are linearly related. The relationship between $\lambda_{N,T}^m$ and the change of surrounding temperature ΔT is as follows

$$\lambda_{N,T}^m = \lambda_T^m + G_T^m \Delta T \tag{12}$$

λ_T^m and $\lambda_{N,T}^m$ are the resonance wavelength dips before and after the surrounding temperature change respectively. In the following part, the surrounding temperature sensing characteristics of the MZI-based sensor under the certain parameters are simulated by FDTD. Parts of the simulation results are

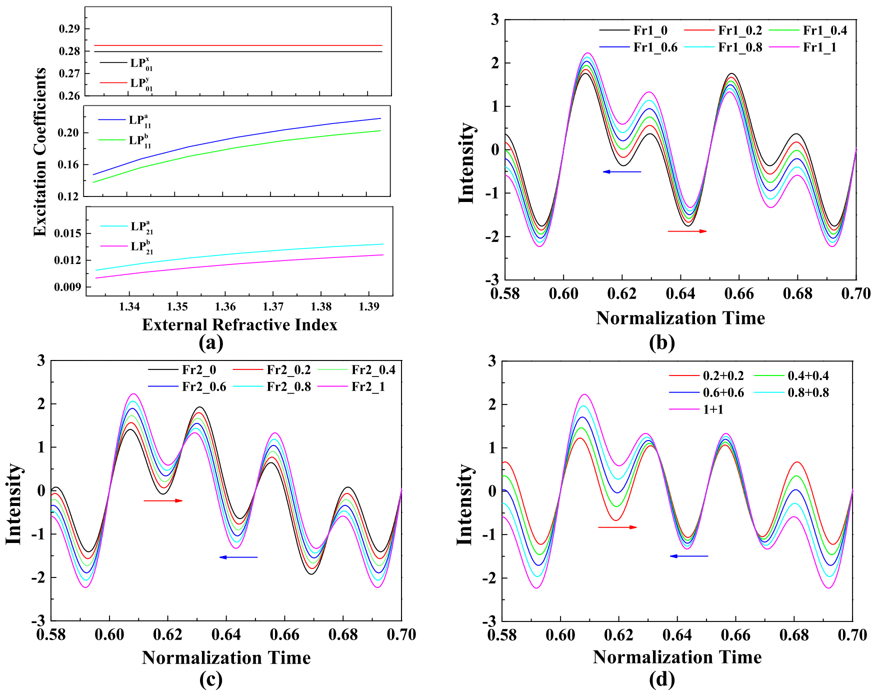

FIGURE 6. **(a) The variation of the excitation coefficients as a function of the external RI changes for different modes; the mixing waveforms with different intensity of (b) frequency 1, (c) frequency 2 and (b) frequency 1 + frequency 2.**

given in the Fig. 5(b) and (d). Fig. 5(b) shows the redshift of the output wavelength line as the temperature in the environment increases (30°, 35°C, 40°C, 45°C, 50°C, 55°C, 60°C, 65°C, 70°C). The corresponding data points are recorded in Fig. 5(d). Our research team find that the linear bivariate associations between the temperature and the two dips are different, which can be seen in the Fig. 5(d). It describes the average surrounding temperature susceptibility of 63 pm/°C and 47.5 pm/°C for dip1 and dip2 respectively. The correlation coefficients R^2 for linear fitting are 0.9999 and 0.9999 respectively. Excellent linearity between the surrounding temperature and wavelength dips is achieved. Due to the different temperature and RI response sensitivities of the two dips, in the absence of temperature cross-sensitivity, SRI could be measured by the proposed MZI-based optical sensor accurately.

From simulation analysis above, it could be seen that these dips are different in drift-direction, drift-sensitivity and intensity for sets of environment variables. As in a previous study, the principle behind it is not discussed in detail. The causes of this phenomenon are diverse, which have been analyzed as shown in Fig. 6. It is shown in this paper that the interference spectrum variation could be realized by adjusting the power ratio of the guide modes in the MZI-based sensor. Fig. 6(a) presents the variation tendency of the mode-excitation coefficient in the sensor with the external RI variation. Since the guide mode, LP_{01}, is trapped in the fiber core, the LP_{01} power in it would be hardly affected by the external RI. In contrast, the LP_{11} and LP_{21} mode group in the fiber cladding is with synchronous change of the external RI, and is sensitive to it. According to the interaction among three low-order modes which are excited in the sensor due to the waveguide property, a stable interference pattern would be caused. The multi-mode interference in this CMCF-based sensor is taken analogous to sinusoids mixing which would be possible to analyze and simulate the spectral shift during SRI or temperature sensing. This pattern could be decomposed into three series of tone which would be distinguished by the frequency, expressed as Frequency 1 (Fr1), Frequency 2 (Fr2) and Frequency 3 (Fr3). With the change of outside condition, the effective refractive indexes of the guide modes in the sensor would have changed slightly, which have a substantial effect to the excitation coefficients of different modes. And then, the intensity of the tones could be tuned by it. Fr1 and Fr2 have been most heavily affected, which has played a great role in the dips shifting. The impact of Fr3 would probably be negligible as its low power proportion. Fig. 6(b)-(d) are the mixing waveforms with different intensity of tones. ‘‘Normalization time’’ presents the timelines of sinusoids. Fig. 6(b) would be got by Fr1 with different intensity + Fr2 with fixed power; Fig. 6(c) would be got by Fr1 with fixed power + Fr2 with different intensity; Fig. 6(d) would be got by Fr1 + Fr2 with different intensity. Fig. 6(b)-(d) present that how the interference spectrum could be subject to variation with different energy ratio of Fr1 to Fr2 which is changing from 0 to 1 with each increase of 0.2. As depicted in Fig. 6(b), the interference spectrum is shifted with the increment of the energy of Fr1. It can be seen that the marked dips show red and blue shifts respectively,

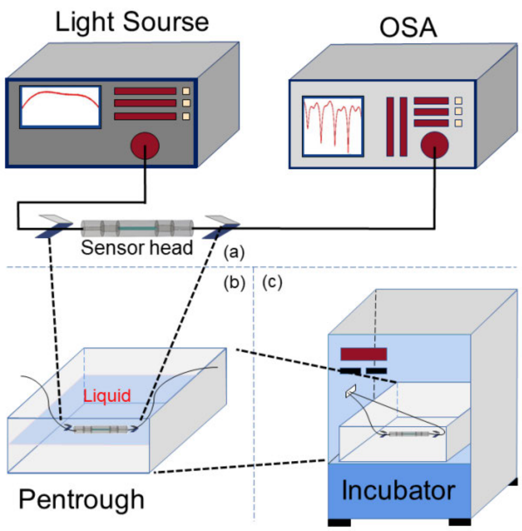

FIGURE 7. **(a) The schematic diagram of experimental setup for (b) RI and (c) temperature measurement.**

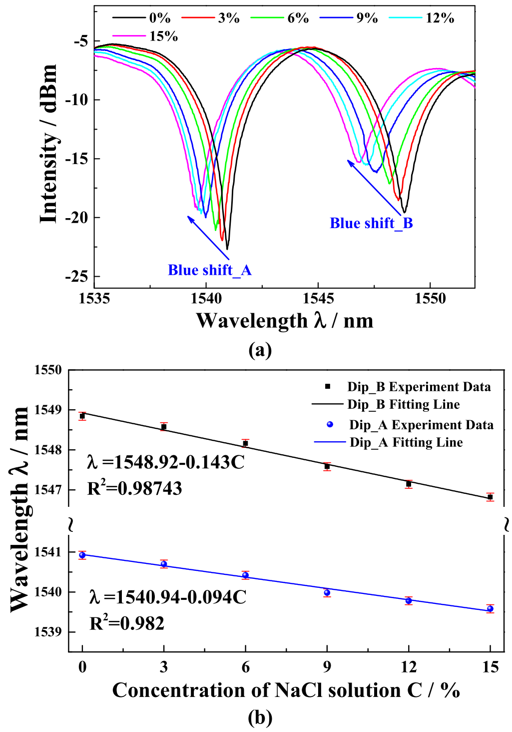

FIGURE 8. **(a) Experimental transmission spectra under different RI of surrounding areas; (b) the fitted result of dips wavelength shifts with different RI.**

and the drift sensitivities are different. It can be seen from Fig.6(c) that the interference spectrum is shifted with the increment of the energy of Fr2. The marked dips show red and blue shifts respectively, however, in which they differed from Fig. 6(b). Fig. 6(d) shows the change of the interference spectrum, which can be connected directly with the adjusting of Fr1 and Fr2. As can be seen from the illustration, the variation in intensity of the tone exerts an independent influence on the drift directions and sensitivities of the dips. However, the whole interference waveform is coupled by these single tones. The drift directions and sensitivities could be flexibly adjusted by the tone intensity. In other words, the waveform drift is ultimately decided by the variation on the n_{eff} of guided modes under their surroundings influence. To sum up, the otherness of the sensitivities and intensities of the dips would be well illustrated.

III. EXPERIMENTAL METHODS AND DISCUSSION

In this experiment, the MZI-based sensor using homemade CMCFs is taken to measure the RI of NaCl solution and the surrounding temperature. Fig. 7 shows the schematic diagram of the sensing experimental setup. An optical spectrum analyzer (OSA) (YOKOGAWA, AQ6375), integrated with a super continuum light source (KOHERAS, superK) which provides an injection light, is used to investigate the output spectrum of this sensor. A pentrough and an incubator are used for RI and temperature sensing respectively.

To prevent and obviate the interferences of temperature and macrobending loss in the SRI sensing experiment, the sensor head is secured with two fiber clips in the pentrough, and placed in the incubator as shown in Fig. 7. The incubator could stability control the temperature around fiber. By adding NaCl to the pentrough, the refractive index of the liquid under test can be changed at room temperature (20°C). With each increase of 3%, the concentration of NaCl in this experiment is changing in 0%-15%, while the SRI increasing from 1.33299 to 1.3609. The corresponding SRIs are measured by an Abbe refractometer, and the measuring approach is references to [28]. Before each measurement, the sensing head must be cleaned up with distilled water and compressed air to make sure the result undisturbed. The results are shown in Fig.8 (a), which describes the blueshift of the central wavelength. SRI and the wavelength of resonance dips are recorded in the Fig.8(b). The correlation coefficients R^2 for linear fitting can reach 0.987, which means that an excellent linearity between SRI and wavelength dips is achieved. It gives average SRI sensitivities of −76.88 nm/RIU and −50.52 nm/RIU separately.

In addition, the linear relationship between the wavelength of resonance dips and the surrounding temperature is also investigated as shown in Fig.7(c). The temperature range measured in this experiment is 0°C-70°C, and record the output result every 5 °C. The results are shown in Fig.9(a). There is a redshift of the central wavelength. The resonance dips and the corresponding temperature are recorded in Fig.9(b). The linear fitting of the experimental data, R^2, is close to 1, and similar to the previous simulation. And it demonstrates that the sensitivity of the surrounding temperature could achieve 80.2nm/°C and 50.1nm/°C respectively. From the experimental results, it is clear that the resonance wavelength dips are different in drift-direction and drift-sensitivity for sets of environment variables. Therefore, this sensor has great potential to temperature-compensated sensing.

Comparing with the simulation result in the same situation, the experimental result provides a sensing feature

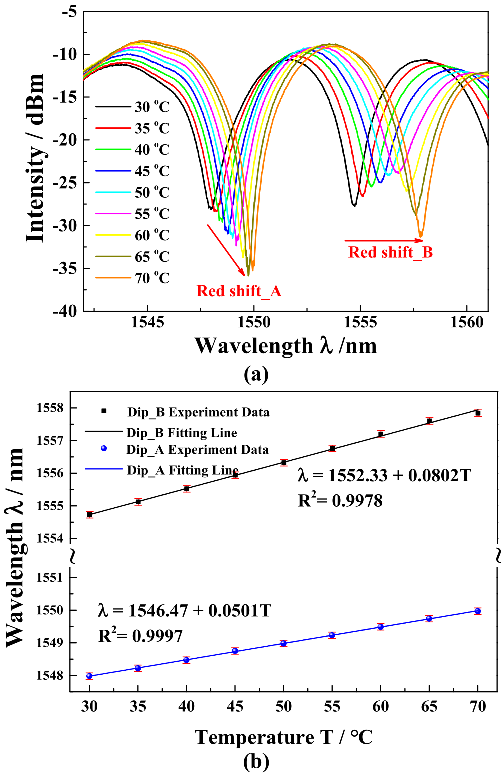

FIGURE 9. (a) Experimental transmission spectra under different temperature of surrounding areas; (b) the fitted result of dips wavelength shifts with different temperature.

consistent with it. Both the emulational and experimental results are uniform in drift-direction, drift-sensitivity and intensity. In both the simulation and experiment, the interference spectrum has a blueshift as the temperature increasing, and the one has a redshift as the SRI increasing. In addition, both the results have good curve fitting characteristics. The sensitivities experimentally achieved are closed to the simulation ones. The SRI sensitivities experimentally achieved are -76.88 and -50.51 nm/RIU, and the temperature ones are 80.2 and 50.1 pm/°C; in the simulation, the SRI sensitivities would be -54.7 and -49.5 nm/RIU, and the temperature ones would be 63 and 47.5 pm/°C. Both in the simulation and experiment, the latter sensitivity, which depends on the n_{eff}^{co} changes, is consistent, and some difference is shown in the former one which depends on the n_{eff}^{cl} changes. The reason of difference would be analyzed as below. From the above discussion in Fig. 3, there are almost only two guided modes in this sensor, and the other high-order modes in cladding is so weak that can be neglected for simplicity. Therefore, in the simulation, the LP_{11} has been considered only. In practice, however, there are some higher modes which would affect the experiment result and not considered in the simulation. Thus, the experimental sensitivity due to the n_{eff}^{cl} changes is higher than the simulation one. The simulation is in order to give the experimental direction, and the proper simplified condition would be desirable. In general, the calculated results are in good agreement with the experimental data.

In practical application, it is impossible to avoid the problem of temperature cross-sensitivity. Traditional RI sensors take advantage of some particular structure or exotic material to guarantee that the sensor head would be insensitive to temperature to mitigate the error. However, through the different response to the SRI and temperature, this MZI-based optical sensor can resolve the temperature cross-sensitivity problem. The accurate SRI can be quantified by solving the two simultaneous equations, (5) and (12). A dual-parameter sensing equation could be got as follows

$$\begin{bmatrix} \Delta\lambda_{N,T}^{m} \\ \Delta\lambda_{N}^{m} \end{bmatrix} = \begin{bmatrix} G_T^m \\ Q_n^m \end{bmatrix} \begin{bmatrix} \Delta T \\ \Delta n \end{bmatrix} \tag{13}$$

where the $\Delta\lambda_{N,T}^{m} = \lambda_{N,T}^{m} - \lambda_{T}^{m}$. The dual-parameter measurement matrix enables the adverse effects of cross-sensitivity to be quantified. When the SRI needs to be accurately measured, we can take advantage of surrounding temperature to compensate the SRI.

In the end, this MZI-based optical sensor using few-mode CMCF has an advantage of getting stable and clean spectrum, high extinction ratio. Combined with wide FSR, the sensor has large range and high resolution. Furthermore, as the output wavelength dips response to surrounding temperature and SRI differently, by analyzing the dual-mode interference process and calculating the dual-parameter measurement matrix, the problem of temperature cross-sensitivity can be resolved. With a terse structure, this sensor is suitable for precise localized measurement.

IV. CONCLUSION

This study sets out to propose and experimentally characterize a temperature-compensated MZI-based optical sensor. The MZI arm in this fiber only supports fundamental mode and LP_{11}, and the excitation coefficients of the two modes are similar. These features ensure stable interferometry and high-quality output images. This specially designed MZI-based optical sensor using few-mode CMCF has well characteristics of being susceptible to the surrounding temperature and SRI. With technology of resonance demodulation, experiments are carried out to analyze its sensing ability. The accurate sensitivity of the response to both SRI and temperature would be obtained. The different sensitivities would enable the temperature-compensated SRI measurement caused by the dual-parameter measurement matrix. Therefore, the sensor system has potential application value in the precision RI measurement system, medical biology and meteorological services.

REFERENCES

[1] D. Fu, X. Liu, J. Shang, W. Sun, and Y. Liu, "A simple, highly sensitive fiber sensor for simultaneous measurement of pressure and temperature," *IEEE Photon. Technol. Lett.*, vol. 32, no. 13, pp. 747–750, Jul. 1, 2020.

[2] Y. Zhang, Z. Chen, W. Chen, and H. Li, "Unobtrusive and continuous BCG-based human identification using a microbend fiber sensor," *IEEE Access*, vol. 7, pp. 72518–72527, 2019.

[3] B. Huang, Y. Wang, C. Liao, and Y. Wang, ''Highly sensitive temperature sensor based on all-fiber polarization interference filter with Vernier effect,'' *IEEE Access*, vol. 8, pp. 207397–207403, 2020.

[4] X. Lei, X. Dong, C. Lu, T. Sun, and K. T. V. Grattan, ''Underwater pressure and temperature sensor based on a special dual-mode optical fiber,'' *IEEE Access*, vol. 8, pp. 146463–146471, 2020.

[5] F. Wang, K. Pang, T. Ma, X. Wang, and Y. Liu, ''Folded-tapered multimode-no-core fiber sensor for simultaneous measurement of refractive index and temperature,'' *Opt. Laser Technol.*, vol. 130, Oct. 2020, Art. no. 106333.

[6] M. A. Mahfuz, M. A. Hossain, E. Haque, N. H. Hai, Y. Namihira, and F. Ahmed, ''Dual-core photonic crystal fiber-based plasmonic RI sensor in the visible to near-IR operating band,'' *IEEE Sensors J.*, vol. 20, no. 14, pp. 7692–7700, Jul. 2020.

[7] D. Yang, Y. Liu, Y. Wang, T. Zhang, M. Shao, D. Yu, H. Fu, and Z. Jia, ''Integrated optic-fiber sensor based on enclosed EFPI and structural phase-shift for discriminating measurement of temperature, pressure and RI,'' *Opt. Laser Technol.*, vol. 126, Jun. 2020, Art. no. 106112.

[8] S. Wu, Q. Tan, E. Forsberg, S. Hu, and S. He, ''*In-situ* dual-channel surface plasmon resonance fiber sensor for temperature-compensated detection of glucose concentration,'' *Opt. Exp.*, vol. 28, no. 14, pp. 21046–21061, Jul. 2020.

[9] S. Weng, L. Pei, C. Liu, J. Wang, J. Li, and T. Ning, ''Double-side polished fiber SPR sensor for simultaneous temperature and refractive index measurement,'' *IEEE Photon. Technol. Lett.*, vol. 28, no. 18, pp. 1916–1919, Sep. 15, 2016.

[10] F. Zhou, H. Su, H.-E. Joe, and M. B.-G. Jun., ''Temperature insensitive fiber optical refractive index probe with large dynamic range at 1,550 nm,'' *Sens. Actuators A, Phys.*, vol. 312, Sep. 2020, Art. no. 112102.

[11] Z. Gong, C. Ke, X. Zhou, and Q. Yu, ''Temperature-compensated refractive index sensor based on bent-fiber interference,'' *Opt. Fiber Technol.*, vol. 36, pp. 6–9, Feb. 2017.

[12] J. S. Velázquez-Gonzélez, D. Monzán-Hernéndez, D. Moreno-Hernández, F. Martínez-Piñén, and I. Hernéndez-Romano, ''Simultaneous measurement of refractive index and temperature using a SPR-based fiber optic sensor,'' *Sens. Actuators B, Chem.*, vol. 242, pp. 912–920, Apr. 2017.

[13] D. F. Santos, A. Guerreiro, and J. M. Baptista, ''Simultaneous plasmonic measurement of refractive index and temperature based on a D-type fiber sensor with gold wires,'' *IEEE Sensors J.*, vol. 17, no. 8, pp. 2439–2446, Apr. 2017.

[14] T. Liu, Y. Chen, Q. Han, F. Liu, and Y. Yao, ''Sensor based on macrobent fiber Bragg grating structure for simultaneous measurement of refractive index and temperature,'' *Appl. Opt.*, vol. 55, no. 4, pp. 791–795, Feb. 2016.

[15] R. Gao and D. Lu, ''Temperature compensated fiber optic anemometer based on graphene-coated elliptical core micro-fiber Bragg grating,'' *Opt. Exp.*, vol. 27, pp. 34011–34021, Nov. 2019.

[16] Y. Ouyang, X. Xu, Y. Zhao, A. Zhou, and L. Yuan, ''Temperature compensated refractometer based on parallel fiber Fabry–Pérot interferometers,'' *IEEE Photon. Technol. Lett.*, vol. 30, no. 13, pp. 1262–1265, Jul. 1, 2018.

[17] P. Jia, G. Fang, T. Liang, Y. Hong, Q. Tan, X. Chen, W. Liu, C. Xue, J. Liu, W. Zhang, and J. Xiong, ''Temperature-compensated fiber-optic Fabry–Pérot interferometric gas refractive-index sensor based on hollow silica tube for high-temperature application,'' *Sens. Actuators B, Chem.*, vol. 244, pp. 226–232, Jun. 2017.

[18] X. Li, S. C. Warren-Smith, L. Xie, H. Ebendorff-Heidepriem, and L. V. Nguyen, ''Temperature-compensated refractive index measurement using a dual Fabry–Pérot interferometer based on C-fiber cavity,'' *IEEE Sensors J.*, vol. 20, no. 12, pp. 6408–6413, Jun. 2020.

[19] H. Lu, Y. Yue, J. Du, L. Shao, T. Wu, J. Pan, and J. Hu, ''Temperature and liquid refractive index sensor using P-D fiber structure-based Sagnac loop,'' *Opt. Exp.*, vol. 26, no. 15, p. 18920, Jul. 2018.

[20] J. Zhao, P. Niu, C. Zhang, X. Sun, H. Bai, and C. Miao, ''Temperature-compensated fiber laser refractometer based on compact hybrid S-taper/FBG structure,'' *Opt. Fiber Technol.*, vol. 45, pp. 300–305, Nov. 2018.

[21] R. Oliveira, J. H. Osório, S. Aristilde, L. Bilro, R. N. Nogueira, and C. M. B. Cordeiro, ''Simultaneous measurement of strain, temperature and refractive index based on multimode interference, fiber tapering and fiber Bragg gratings,'' *Meas. Sci. Technol.*, vol. 27, Jun. 2016, Art. no. 075107.

[22] Y. Ju, S. Ning, H. Sun, J. Mo, C. Yang, G. Feng, H. Zhou, and S. Zhou, ''Temperature and refractive index measurement based on a coating-enhanced dual-microspheric fiber sensor,'' *Laser Phys.*, vol. 28, no. 7, May 2018, Art. no. 076203.

[23] X. Hu, X. Shen, J. Wu, J. Peng, L. Yang, J. Li, H. Li, and N. Dai, ''All fiber M-Z interferometer for high temperature sensing based on a hetero-structured cladding solid-core photonic bandgap fiber,'' *Opt. Exp.*, vol. 24, no. 19, p. 21693, Sep. 2016.

[24] L. Zhang, D. N. Wang, J. Liu, and H. F. Chen, ''Simultaneous refractive index and temperature sensing with precise sensing location,'' *IEEE Photon. Technol. Lett.*, vol. 28, no. 8, pp. 891–894, Apr. 15, 2016.

[25] M. M. Ali, Y. Jung, K.-S. Lim, M. R. Islam, S.-U. Alam, D. J. Richardson, and H. Ahmad, ''Characterization of mode coupling in few-mode FBG with selective mode excitation,'' *IEEE Photon. Technol. Lett.*, vol. 27, no. 16, pp. 1713–1716, Aug. 15, 2015.

[26] X. Liang, Y. Li, Z. Geng, and Z. Liu, ''Selective transverse mode operation of a fiber laser based on few-mode FBG for rotation sensing,'' *Opt. Exp.*, vol. 27, pp. 37964–37974, Dec. 2019.

[27] J. Zuo, T. Han, J. Yang, Y. Chen, Y.-G. Lin, and J. Cai, ''High sensitivity temperature sensor with an avoided-crossing based selective-filling high birefringent photonic crystal fiber Sagnac interferometer,'' *IEEE Access*, vol. 6, pp. 45527–45533, 2018.

[28] G. Yin, S. Lou, and H. Zou, ''Refractive index sensor with asymmetrical fiber Mach–Zehnder interferometer based on concatenating single-mode abrupt taper and core-offset section,'' *Opt. Laser Technol.*, vol. 45, pp. 294–300, Feb. 2013.

BIN-ZHOU ZUO was born in Leshan, Sichuan, China, in 2000. He is currently pursuing the bachelor's degree in optoelectronic information science and engineering with the Minzu University of China. He obtained a scholarship for the first two years. He had won more than ten prizes at the provincial level. His research interests include high-accuracy fiber optic sensors, semiconductor low-dimensional materials, and computer vision with artificial intelligence.

XIAO LIANG was born in Handan, Hebei, China, in 1985. He received the Ph.D. degree in communication engineering from Beijing Jiaotong University, Beijing, China, in 2016.

From 2017 to 2020, he was a Research Assistant with the Minzu University of China. Since 2020, he has been an Assistant Professor with the School of Information Engineering, Minzu University of China. His research interests include optical fiber sensing and high-speed optical communication systems.

XU-RAN ZHANG was born in Xuzhou, Jiangsu, China, in 2000. He is currently pursuing the bachelor's degree in communications engineering with the Minzu University of China. He has outstanding performance in both professional courses and academic competitions, as well as comprehensive practical skills. He has also enhanced his knowledge by constant learning. His research interests include optical fiber sensing and high-speed optical communication systems.

TIAN-HE YIN was born in Chengdu, Sichuan, China, in 2001.

He is currently a Sophomore Student majors in English translation at the Minzu University of China. He has achieved excellent grades in schoolwork and won the national scholarship as a freshman. He is also equipped with interdisciplinary knowledge. He has made considerable contribution to the translation of this article.